LA-14499

Overview of Liquid-Solid Reaction Mechanisms and Kinetics of MBe_{13} Formation for Lanthanide-Beryllium and Actinide-Beryllium Systems

Los Alamos
NATIONAL LABORATORY
EST.1943

Los Alamos National Laboratory, an affirmative action/ equal opportunity employer, is operated by Los Alamos National Security, LLC, for the National Nuclear Security Administration of the U.S. Department of Energy under contract DE-AC52-06NA25396.

LA-14499
Issued: April 2018

Overview of Liquid-Solid Reaction Mechanisms and Kinetics of MBe_{13} Formation for Lanthanide-Beryllium and Actinide-Beryllium Systems

Samantha K Lawrence, Sigma-2[1]

Robert E. Hackenberg, Sigma-2[1]

Thomas G. Zocco, W-DO[1]

Robert Hanrahan[2]

[1] Los Alamos National Laboratory, Los Alamos, NM
[2] NNSA Headquarters, Washington, D.C.

Los Alamos
NATIONAL LABORATORY
EST.1943

Abstract

Molten rare-earth elements form intermetallic compounds with solid beryllium of the form MBe_{13}, where M represents any of the rare-earth metals (lanthanides). Importantly, an intermetallic compound with the same stoichiometry is formed between liquid plutonium and solid beryllium. These lanthanide and actinide intermetallic compounds are of interest because of their high melting points (in excess of 1500°C) and simple (cubic) crystallographic lattice. Despite the possible useful properties of these intermetallic compounds, the kinetics and thermodynamics of their formation have not been well quantified. A series of experiments was performed at Los Alamos National Laboratory in the 1990s in an attempt to ascertain the mechanism responsible for intermetallic formation in a variety of lanthanide-beryllium and actinide-beryllium combinations. These data are reviewed and analyzed in the present report. A kinetic analysis is applied where possible to compare interactions between solid beryllium and molten lanthanum, cerium, praseodymium, samarium, and ytterbium; these results are further compared with data collected for the plutonium-beryllium system.

Page intentionally blank

Table of Contents

Page intentionally blank

List of Figures

Page intentionally blank

List of Tables

Page intentionally blank

1 Introduction

Unusual circumstances could result in contact between molten Pu and solid Be components. Since intimate contact between Pu and Be results in an intense neutron source via the alpha particle-neutron (α,n) reaction, it is difficult to study the kinetics of the Pu-Be interaction. The published Pu-Be phase diagram [1] is characterized by a single intermetallic compound, $PuBe_{13}$, which exists in equilibrium with all of the Pu allotropes, and two eutectics with no measurable solubility range in any of the solid phases (Figure 1a). This pattern is known to be followed by all of the rare-earth elements (lanthanides) and some of the actinides. Although most of the phase diagrams for those lanthanides and actinides are poorly defined in terms of solubility and eutectic location, all have been characterized to the extent of having a single intermetallic compound with a melting point in excess of 1500°C. Consequently, studying the reactions of these other lanthanide metals with Be should make it possible to bound kinetics and mechanisms of the Pu-Be interaction using known physical and thermodynamic properties.

Even with a lack of complete phase diagrams for interaction between the lanthanides and Be, a single high-melting intermetallic compound with stoichiometry MBe_{13}, (where M is used to refer to any of the rare-earth metals) has been identified in every case. The lanthanide MBe_{13} and $PuBe_{13}$ intermetallic compounds are isostructural, bearing an $Fm\overline{3}c$ space group, a face-centered cubic crystal structure, a composition of 92.9 at. % Be and are prototyped by the $NaZn_{13}$ intermetallic.

Despite the similarities among the lanthanide-Be and Pu-Be intermetallic compounds, lanthanides differ from Pu in a number of key ways. The most obvious difference between Pu and lanthanide elements is in their melting points (see Table I). This is not the most important consideration, however, due to the presence of two eutectics in each of the M-Be systems. Additionally, the atomic numbers (and thus electronic structure) and lattice parameters of the lanthanides vary significantly from Pu (values are collected in Table I).

This report discusses new analysis of experiments conducted at Los Alamos National Laboratory (LANL) during the 1990s to ascertain the controlling kinetic parameters in six lanthanide-Be systems: Yb-Be, Sm-Be, Ce-Be, Pr-Be, La-Be, and CeGa-Be (existing phase diagrams are shown in Figure 1). Calculation of the reaction rate constant was possible only for the Yb-Be, Sm-Be, Ce-Be, and Pr-Be systems, so only these couples are compared directly. Comparison of available data on $PuBe_{13}$ formation with that of lanthanide MBe_{13} formation lends insight into the

feasibility of using kinetic models generated from lanthanide intermetallic formation to predict reaction rates and mechanisms for the Pu-Be system or other actinide-Be systems.

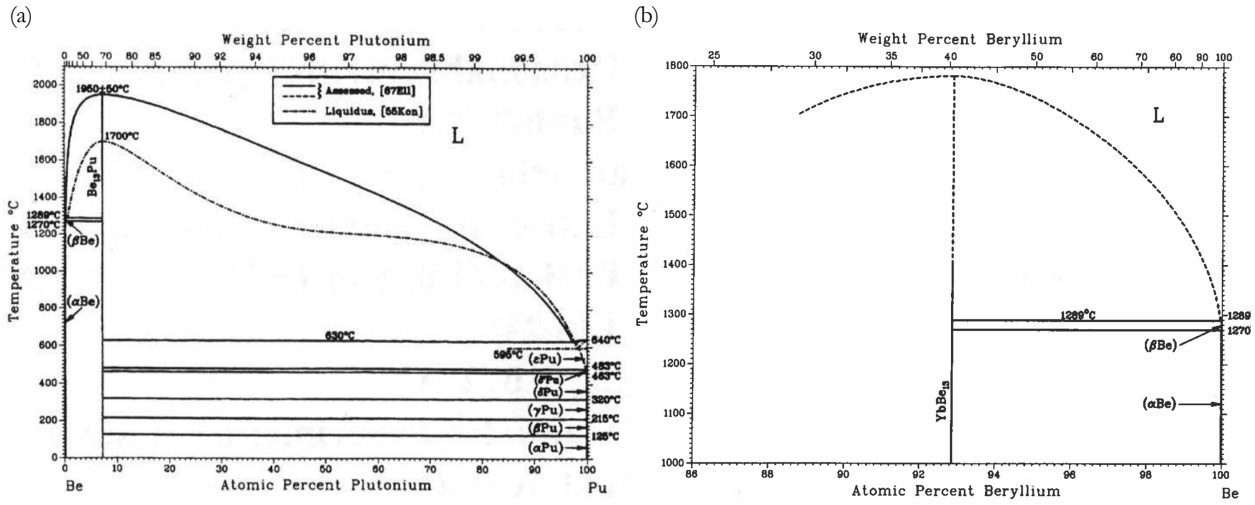

Figure 1. Phase diagrams for (a) Pu-Be and (b) Yb-Be.

Table 1. Select Characteristics of the Lanthanides and Actinide Used in This Study.
*From *[2]*, #From *[3]*.

Metal Element	**Atomic Number**	**Melting Temperature (˚C)**	**Electronic Configuration (μm)**	**Lattice Parameter of Beryllide (Å)**
La	*57*	920	$[Xe]6s^25d^1$	10.451*
Ce	*58*	795	$[Xe]6s^24f^15d^1$	10.372*
Pr	*59*	919	$[Xe]6s^24f^3$	10.369*
Sm	*62*	1070	$[Xe]6s^24f^6$	10.304*
Yb	*70*	824	$[Xe]6s^24f^{14}$	10.180*
Pu	*94*	639.5	$[Rn]7s^25f^6$	10.282#

2 Experimental Procedures

2.1 1990s Lanthanide-Beryllium Experiments

In order to study the kinetics of M-Be (where M indicates one of the lanthanides) reactions, a series of experiments was conducted [4] in which Be crucibles were filled with solid M and subsequently held at temperatures from 800° to 1200°C in flowing argon for various times. Three sizes of Be crucibles were used in the reaction experiments in order to vary the surface area to volume (S/V) ratio of the M and Be. Approximately 1/2 to 2/3 of the crucible volume was filled with solid metal, resulting in S/V ratios of 1.6, 2.6, and 5.9 [4]. The crucible was then placed in a vacuum tube furnace which was evacuated and filled with ultrahigh-purity (UHP) argon. The furnace was heated at a rate of 16.6°C/min, held at temperature for times ranging from 5 min to 10 hr and furnace cooled. After the exposure was completed the crucible was sectioned using a low speed diamond saw; mounted, ground, and polished using appropriate metallographic techniques; and imaged using backscattered electrons (BSEs) in a scanning electron microscope (SEM). The kinetics and mechanism of the reaction were determined based on the thickness of the reaction layer at the interface between the M and Be, the depth of penetration (if visible) of the MBe_{13} reaction layer into the Be, the morphology of the interface, and the amount and distribution of intermetallic precipitates in the solidified metal, all as a function of exposure temperature and time.

2.2 1990s Plutonium-Beryllium Experiments

Pu-Be experiments were conducted [5] using Be crucibles with samples yielding a S/V of 2.2. Crucibles were machined from S200D powder–processed Be stock and coated with CaF_2 paint to avoid wetting of the Be during the test. Figure 2 shows the crucible and thermocouple geometry. Tests were conducted using a resistively heated vacuum furnace in the Plutonium Facility at LANL; the vacuum environment was achieved using a cryo pump and a limited-volume chilled water supply. Samples were heated at 40°C/min, 30°C/min, or 15°C/min to 1000°C, 1100°C, or 1200°C and held for various times; temperature data were collected every 2–15 sec (depending on test duration). Additionally, neutron count was monitored using a Canberra Neutron Detection system because the interaction between alpha particles generated by Pu decay and Be atoms produces a significant number of neutrons (the α-n reaction) [6]. Note that a runaway reaction, which occurs when the excess neutrons created by the α-n reaction lead to the creation of a critical mass of Pu, was never observed [5]. After the exposure was completed, the crucible was sectioned using a low-speed diamond saw; mounted, ground, and polished using appropriate metallographic techniques; and imaged using backscattered electrons in a SEM.

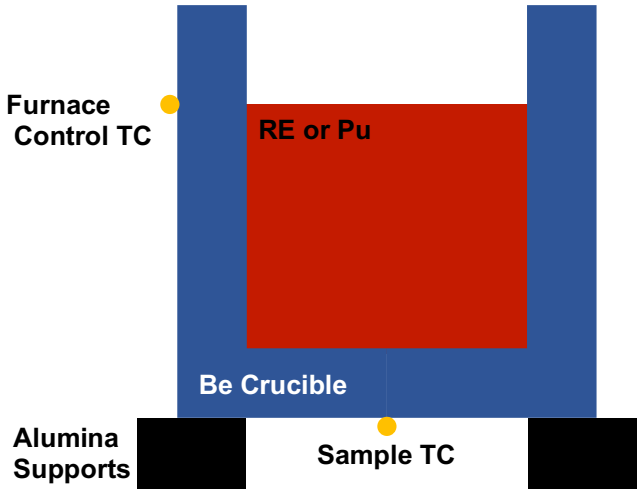

Figure 2. Test configuration for all Pu tests.

3 Results

3.1 MBe_{13} Intermetallic Morphologies

Figure 3-Figure 6 present backscatter electron images of the MBe_{13} intermetallic compounds formed when Ce (Figure 3), Sm (Figure 4), Yb (Figure 5), and Pr (Figure 6) are melted in Be crucibles. In all images, the black regions near the edges are the Be crucibles, and the light grey interiors are solidified metals, while the intermetallic layer, between the crucible and solidified metal, appears dark grey.

All four MBe_{13} layers are similar in that the thickness of the intermetallic is about the same on both the bottom and sides of the crucible. While the layer thickness decreases slightly around the corners in some systems, they are always coated. The morphology of the compounds does not vary appreciably with exposure temperature for a given metal. In contrast, the morphology does vary among the rare-earth metals tested. In particular, $YbBe_{13}$ does not form obvious faceted dendrites at the Yb-intermetallic interface, as are apparent in the $CeBe_{13}$, $SmBe_{13}$, and $PrBe_{13}$ compounds. The Yb-Be system also differs from the other M-Be systems in that significant porosity forms behind the $YbBe_{13}$ intermetallic, at the interface with the Be crucible.

In comparison, the $PuBe_{13}$ intermetallic displays morphological aspects in common with multiple M-Be systems. Specifically, significant porosity is observed at the intermetallic-Be interface (Figure 7b), while large faceted dendrites are also apparent (Figure 7a-b). The large faceted particles at the interface are considerably more numerous after the longer exposure, and many more appear in the solidified material. These appear to have broken off from the wall and floated to the top of the

melt. Fine particles of $PuBe_{13}$ (not visible here) appear distributed throughout the solidified Pu. These most likely precipitated during cooling of the Pu as the solubility of Be in the molten or solid Pu decreased.

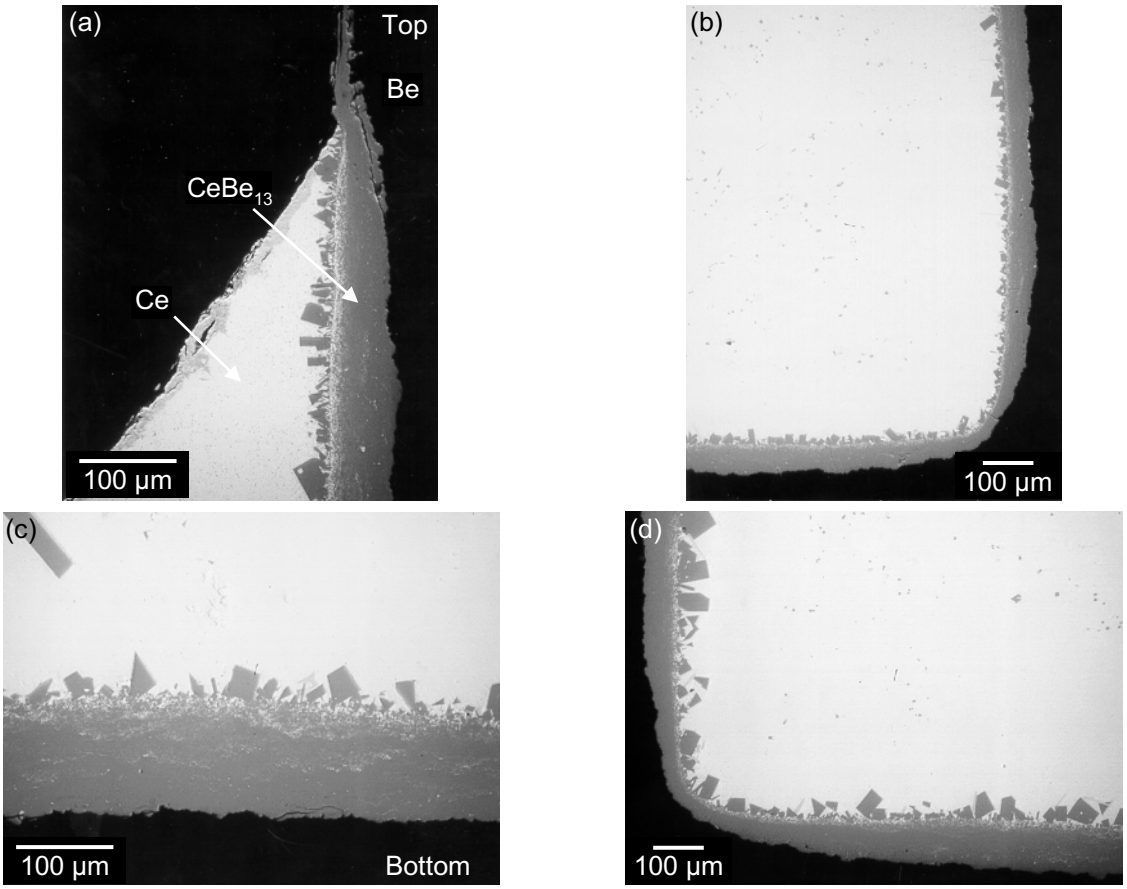

Figure 3. BSE images of the $CeBe_{13}$ layer formed upon cooling of molten Ce in a Be crucible. The intermetallic grows into the crucible wall (a). Blocky dendrites form at the liquid-solid interface after exposure at 1000˚C (a-b) and 1100˚C (c-d) for 60 min. Intermetallic thickness decreases slightly at the corners (b, d). Crucibles are oriented vertically in all images. The top of the image corresponds with the upper portions of the crucible; the bottom of the image corresponds with the crucible bottom.

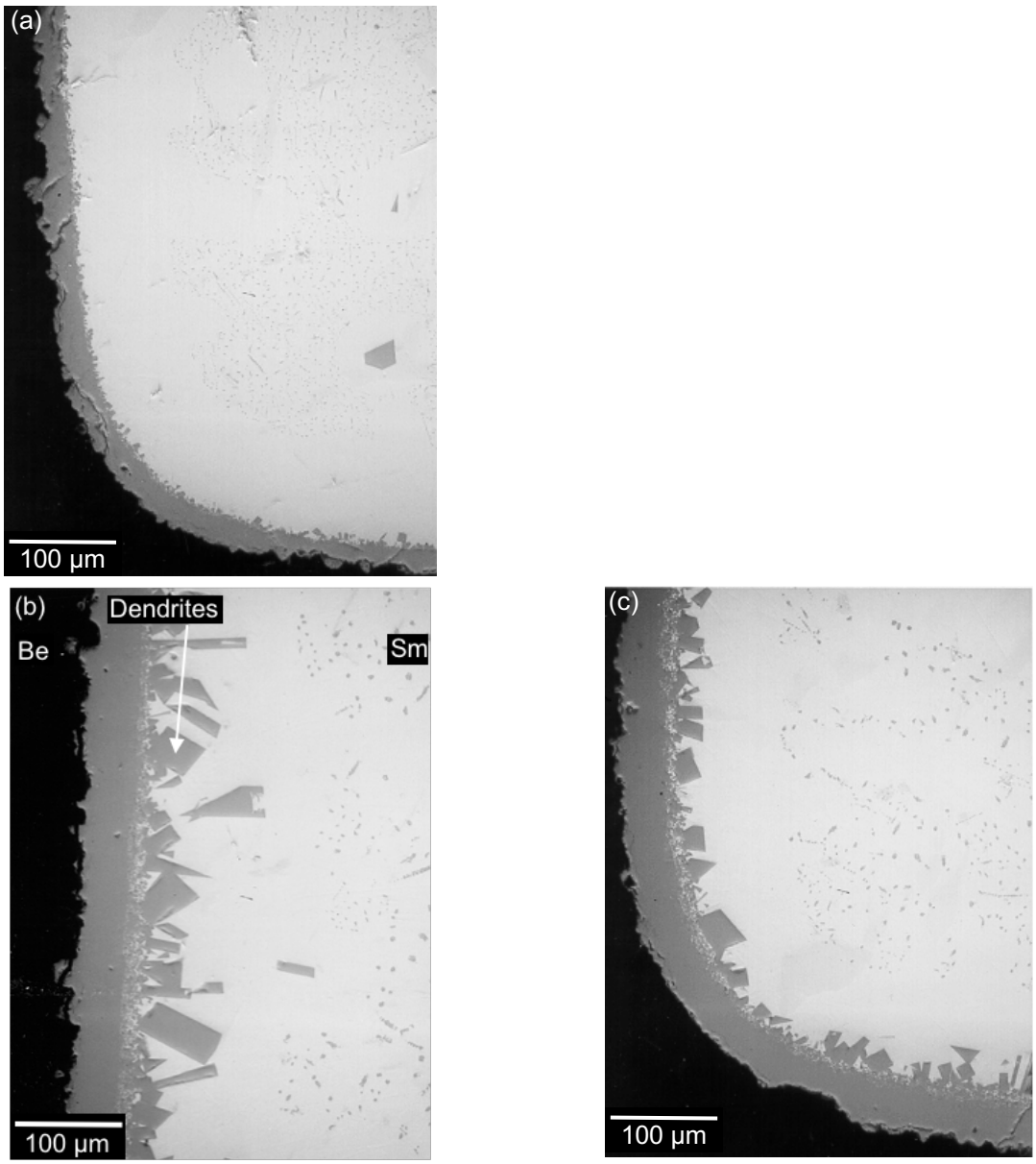

Figure 4. BSE images of the $SmBe_{13}$ layer formed upon cooling of molten Sm in a Be crucible. Blocky dendrites form at the liquid-solid interface after exposure at 1000°C for 60 min (a) and 1100°C for 60 min (b-c). The thickness of the intermetallic does not change appreciably at the corners in this system (a,c). The crucible is oriented vertically in each image.

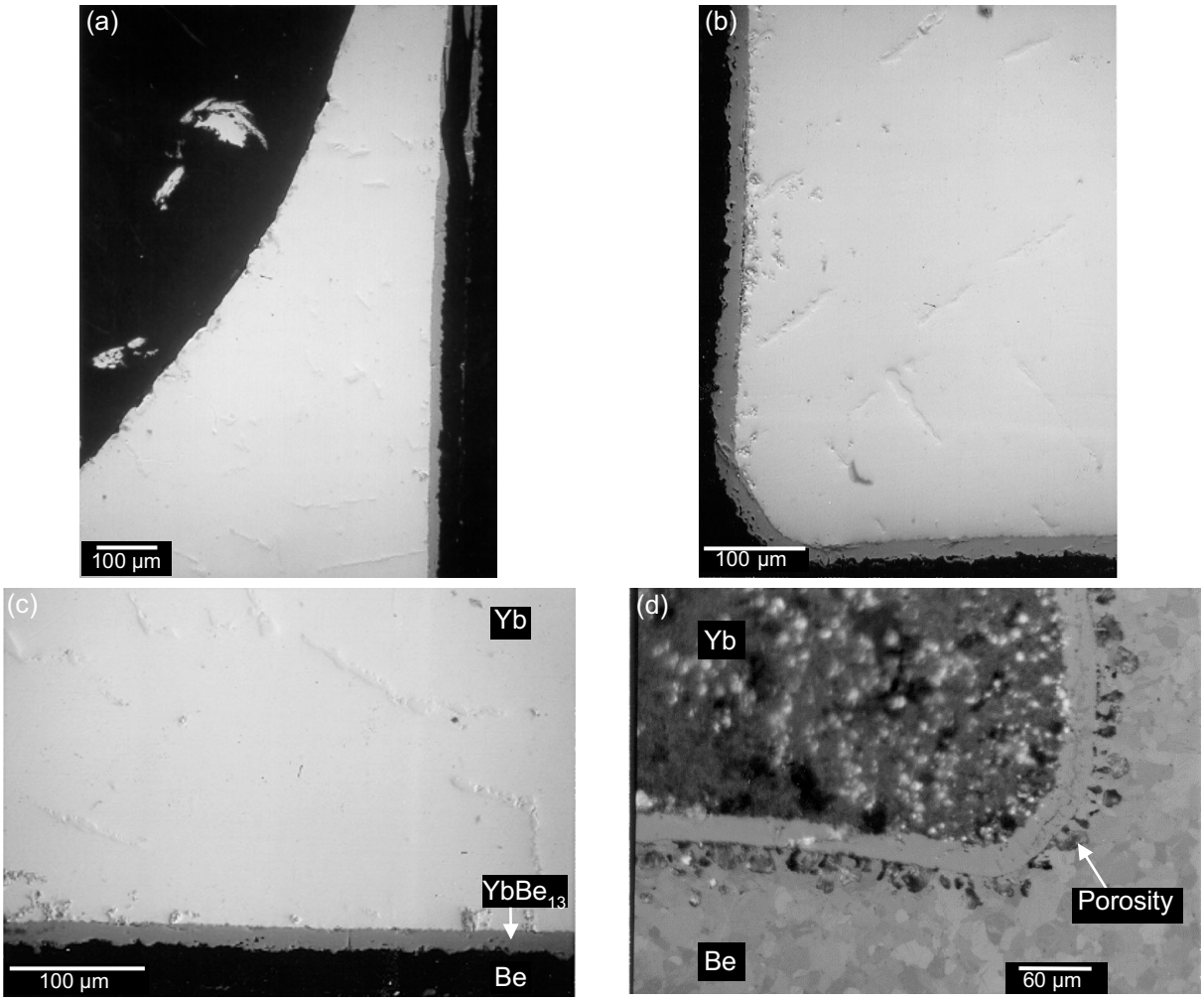

Figure 5. BSE images of the $YbBe_{13}$ layer formed upon cooling of molten Yb from 1200°C after a 5-min hold in a Be crucible (a-c) and a light optical image of the intermetallic formed upon cooling from 1000°C (d). The optical micrograph shows the significant porosity that forms along the Be-intermetallic interface, which is not visible in the BSE images due to poor contrast from the Be. Note that micrographs from a 1200°C exposure are shown because no original high-quality micrographs of lower temperatures could be found. Crucibles are oriented vertically in all images.

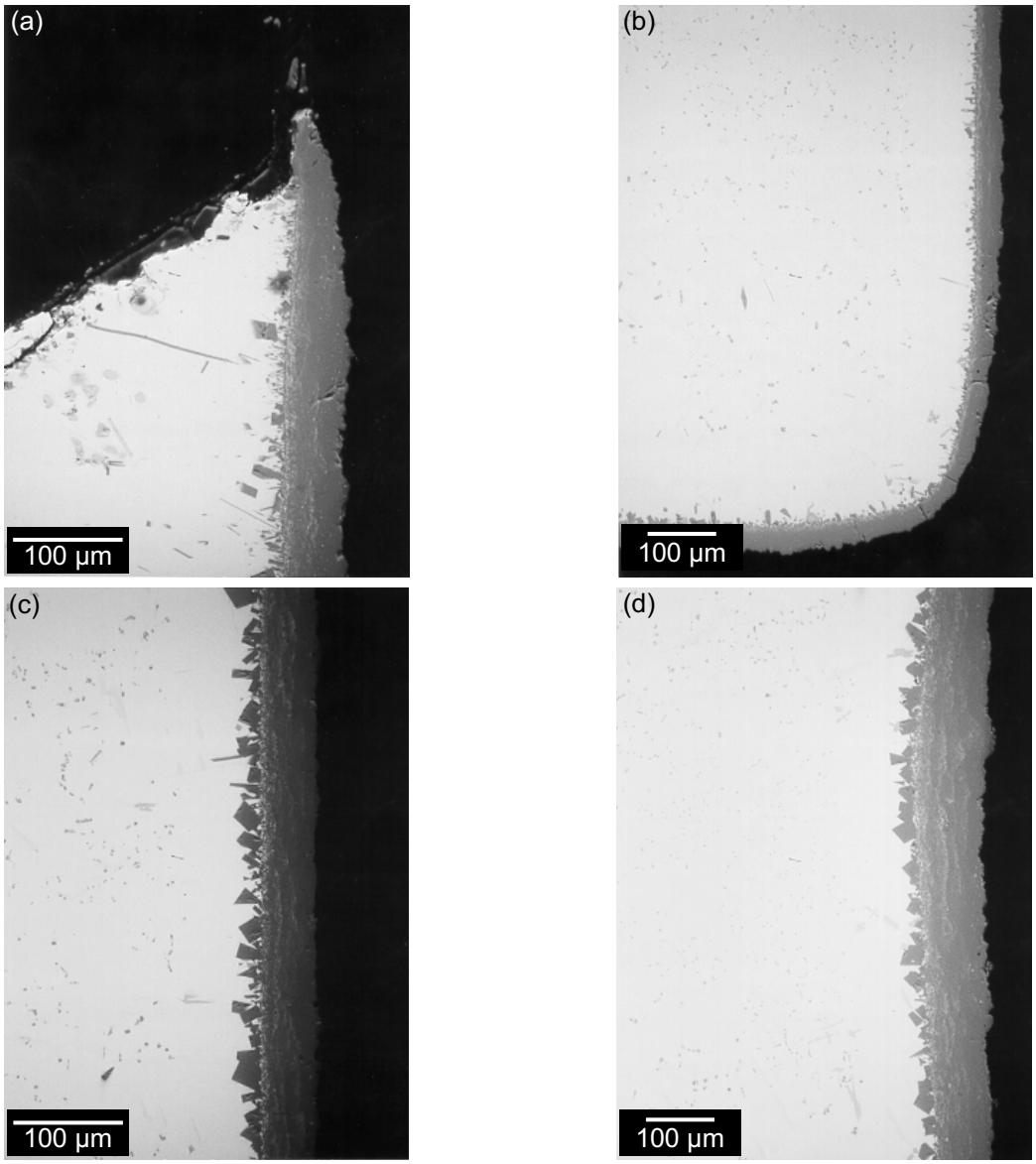

Figure 6. BSE images of the $PrBe_{13}$ layer formed upon cooling of molten Pr in a Be crucible. The intermetallic grows into the Be crucible wall (a). Blocky dendrites form at the liquid-solid interface after exposure at 1000˚C for 60 min (a-b) and 1100˚C for 60 min (c-d). The thickness of the intermetallic does not change appreciably at the corners in this system (b). Crucibles are oriented vertically in all images.

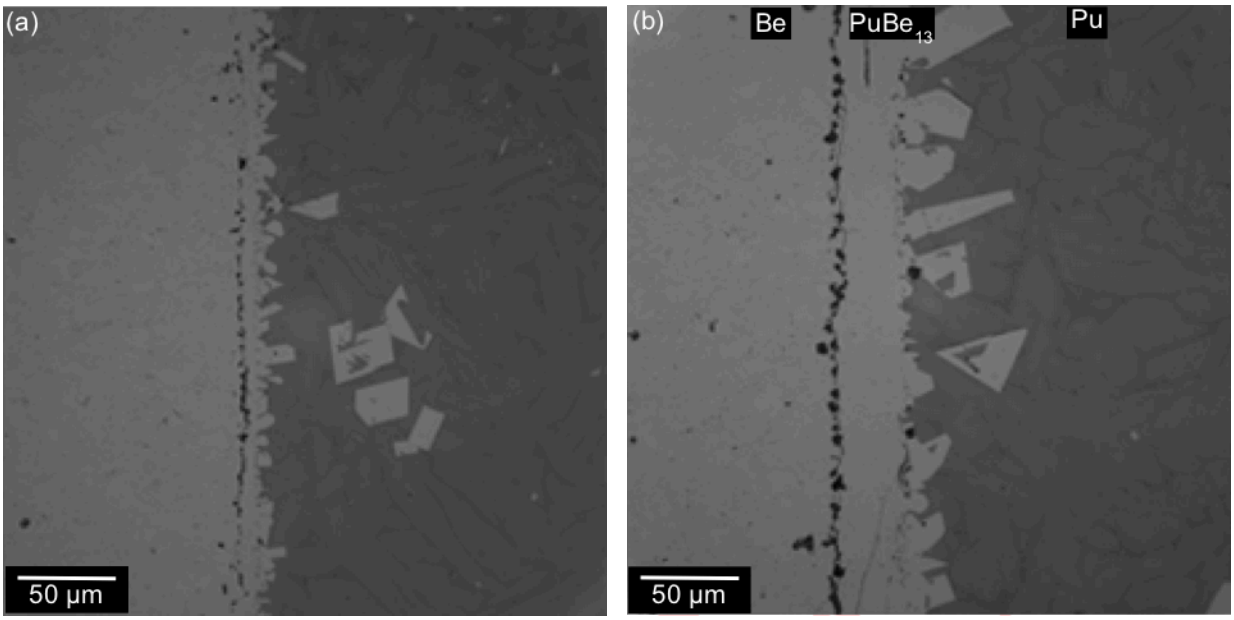

Figure 7. BSE images of the $PuBe_{13}$ layer formed upon cooling of molten Pu in a Be crucible after (a) a 5-min hold at 1000°C and (b) a 7-hour hold at 1000°C. Significant porosity is evident along the interface between the Be crucible and the $PuBe_{13}$. Blocky dendrites are visible in both images.

3.2 Kinetic Analysis of Intermetallic Formation

The first step in conducting a kinetic analysis of the intermetallic growth data is to determine the controlling kinetic regime for each reaction. Measured MBe_{13} thickness is plotted as a function of exposure time for each exposure temperature; these data are then fit using a standard empirical power law relationship of the form [6]

$$h = Kt^n, \qquad \text{(Eq. 1)}$$

where h is the intermetallic layer thickness and the exponent n on time, t, describes the controlling reaction. Exponents near 0.3 indicate grain boundary diffusion control, exponents near 0.5 indicate bulk diffusion control, and exponents near 1.0 indicate interface control. Once the time exponent has been determined, the reaction rate constant, K, for each regime can then be calculated. Finally, the activation energy for a particular kinetic process can be calculated using both the K and n values.

3.2.1 Determination of Controlling Kinetic Regime

The controlling kinetic regimes for the growth of four lanthanide-Be intermetallic layers were calculated and directly compared. The thickness of the intermetallic layer formed by melting Ce, Sm, Yb, and Pr in Be crucibles was measured as a function of time at temperature (values tabulated in Appendix I, Table A1). The raw thickness vs. time data measured at 1000°C and 1100°C are plotted

for each lanthanide-Be intermetallic in Figure 8a. The lines of best fit through each data set correspond to a linear transformation of the log-log fit, based on the log transformation of Eq. 1:

$$logh = logK + nlogt. \quad \text{(Eq. 2)}$$

This log-log fitting procedure is used only to directly determine and compare the time constant, *n*.

As shown in Figure 8a, *n* values range between 0.51 and 1.1 for the lanthanide-Be systems investigated, suggesting that intermetallic growth is controlled either by bulk atomic diffusion through the intermetallic (in the case of Sm, Yb) or by the reaction between the liquid lanthanide and solid Be/intermetallic (in the case of Pr). The time exponent for Ce-Be held at 1000˚C is 0.72, which would suggest a crossover regime. However, given the small number of data points used to calculate this curve, the lack of repeat measurements, and the fact that the Ce-Be system held at 1100˚C has *n*=0.5, a crossover regime seems unlikely. Given the suspect nature of the time exponent, the 1000˚C Ce-Be data were fit again, this time forcing the time exponent to be 0.5, as shown in Figure 8b. The fit is adequate at short times and will be used going forward.

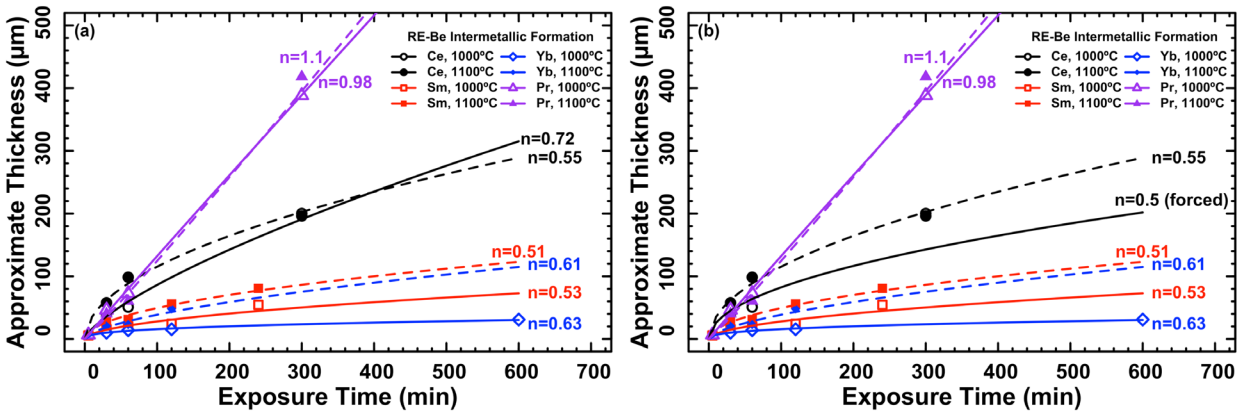

Figure 8. Thickness as a function of exposure time for four rare-earth (RE)-Be intermetallic layers formed during thermal treatments at 1000˚C and 1100˚C.

3.2.2 Determination of Reaction Rate Constant under Diffusion Control

As evident in Figure 8, the time exponent values fall into two groups: those that are roughly 0.5 (diffusion controlled) and those that are approximately 1.0 (interface controlled). The reaction rate constant for these two groups of data will be determined separately. First, the thickness data for the diffusion-controlled growth of $CeBe_{13}$, $YbBe_{13}$, and $SmBe_{13}$ are plotted against $t^{1/2}$ in Figure 9. Note that the units for thickness and time have been converted to meters and seconds, respectively. These data are then fit with a simple diffusion-controlled layer growth model to determine the layer growth coefficient (i.e., reaction rate coefficient), *K*:

$$h = h_0 + \sqrt{Kt}. \qquad \text{(Eq. 3)}$$

In the above equation, h is the intermetallic layer thickness at time t; h_0 is the initial layer thickness (in this case, always 0 m). The layer growth constant is determined by a linear regression analysis of h vs $t^{1/2}$; these fits are shown in Figure 9 as solid and dashed lines, for 1000°C and 1100°C exposures, respectively.

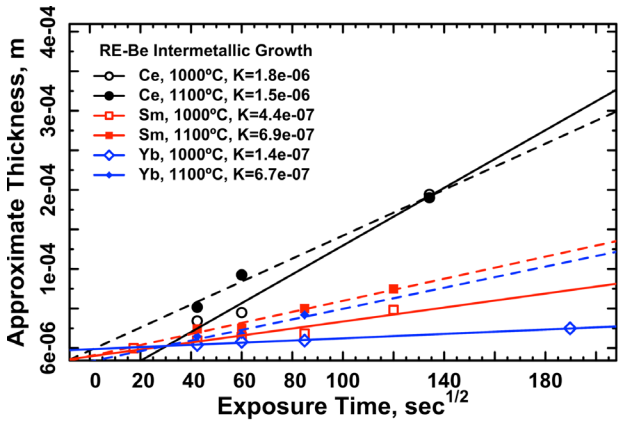

Figure 9. Parabolic growth kinetics curves for $CeBe_{13}$, $SmBe_{13}$, and $YbBe_{13}$ intermetallic layers. The slopes, m, are equivalent to the growth rate coefficient, K.

3.2.3 Determination of Reaction Rate Constant under Interface Control

The growth of $PrBe_{13}$ exhibits interface control (n=1) rather than diffusion control. In this case the thickness vs. time data (in meters and seconds) are plotted on linear axes in Figure 10, and a simple linear regression is applied to determine the reaction rate constant, K.

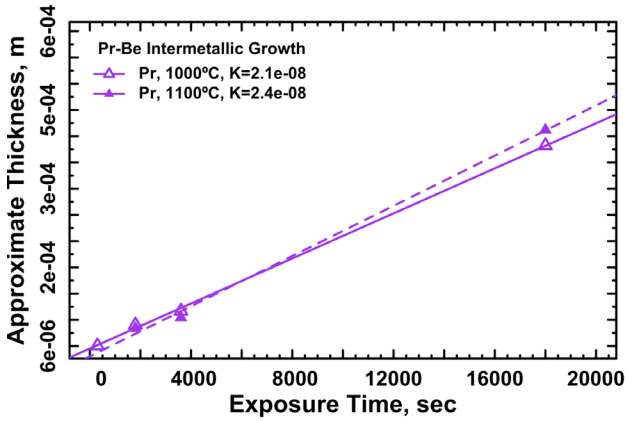

Figure 10. Linear growth kinetics curves for the $PrBe_{13}$ intermetallic. The slopes, m, are equivalent to the growth rate coefficient, K.

3.2.4 Compilation of Kinetic Values

The time exponents, *n*, calculated by fitting MBe_{13} growth data with Eq. 2 and the reaction rate constants, *K*, determined using linear regression of the data in Figure 9 and Figure 10 are collected in Table *2* for ease of comparison. Activation energies for intermetallic formation were not calculated because a statistically significant value cannot be determined with only two temperatures.

Table 2. Calculated Time Exponents and Reaction Rate Constants for the Lanthanide Intermetallic Layers.

Lanthanide Intermetallic	Exposure Temperature (˚C)	Time Exponent, *n*	Controlling Regime	Reaction Rate Constant, *K* (m/s^n)
$CeBe_{13}$	*1000*	0.72	Diffusion, forced	1.8×10^{-6}
	1100	0.55	Diffusion	1.5×10^{-6}
$SmBe_{13}$	*1000*	0.53	Diffusion	4.4×10^{-7}
	1100	0.51	Diffusion	6.9×10^{-7}
$YbBe_{13}$	*1000*	0.63	Diffusion	1.4×10^{-7}
	1100	0.61	Diffusion	6.7×10^{-7}
$PrBe_{13}$	*1000*	0.98	Interface	2.1×10^{-8}
	1100	1.1	Interface	2.4×10^{-8}

3.3 Effect of Crucible Size

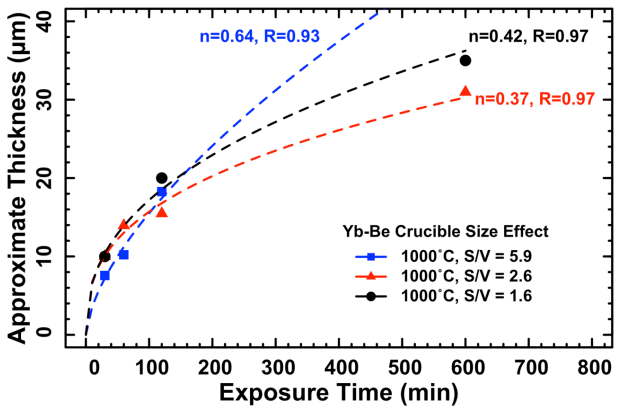

Figure 11. Intermetallic thickness as a function of exposure time for Yb melted in Be crucibles with three different surface-to-volume ratios.

Intermetallic growth experiments at 1000˚C were conducted using three different crucible sizes for the Yb-Be system only [8]. Varying the size of the Be crucible, while keeping the quantity of lanthanide constant results in a variation of the S/V ratio. Three S/V ratios were tested: 5.9 m^{-1}, 2.6 m^{-1}, and 1.6 m^{-1}. Intermetallic thickness is plotted as a function of time in Figure 11; the data are fit to Eq. (1) to determine the *n* values as a function of S/V ratio. The time exponents indicate diffusion control for S/V ratios of 1.6 and 2.6, while the rate controlling step for the S/V=5.9 crucible is more ambiguous. A value of n=0.63 is obtained, but the layer thickness at an exposure time of 600 sec could not be measured for this crucible. The original reports note that "all Yb was

lost" during this test [8]. The lack of a data point at this longest time makes the data fit less comparable with the other crucibles.

3.4 Beryllium Attack

In addition to intermetallic formation, exposure of solid Be to certain molten lanthanides causes Be attack; that is, the lanthanide atoms are defused, and growth of the intermetallic into the Be predominates. This type of behavior is observed when Be is exposed to molten Ce, Pr, and La. Measuring the in-growth, or penetration depth, of the intermetallic layer into the Be crucible wall is one method for estimating attack rates. Such measurements were made using micrographs that show the meniscus of solidified intermetallic and lanthanide, highlighting the penetration depth into the Be wall; this type of feature can be seen in Figure 3a and Figure 6a. Note, however, that the penetration depth does not equal the MBe_{13} thickness; in most cases the intermetallic both penetrates the Be wall and grows outward from the Be into the melt. Intermetallic thickness and penetration depth measurements are collected in Table A1 and A2, respectively.

Two methods are available for estimating attack rate based on penetration depth vs. time data. First, the penetration depth of the intermetallic into the Be wall is plotted as a function of exposure time in Figure 12. Linear regression is applied to these data; the slopes of the lines are lower bound attack rates of Be by each lanthanide. Recognize that only two times at each temperature are shown, due to a lack of micrographs from which penetration depth could be measured; hence, the kinetics may not truly be linear. The estimated attack rates are listed on Figure 12; due to a lack of data no clear trend is evident. Note that the rate calculated for Ce held at 1000°C is considerably higher than that calculated for Ce at 1100°C; this is likely an outlier effect, similar to that observed when calculating the time exponents for $CeBe_{13}$ formation.

The second method for estimating the Be attack rate is to simply take the ratio of the penetration depth to exposure time at each data point (the raw data are collected in Table A2). In this case the attack rates are slightly higher than those calculated with linear regression. Ce appears to be the most reactive lanthanide, with a maximum attack rate of ~2 μm/min at 1100°C, but the attack rates for all three lanthanides are generally low.

Finally, it is important to note that Be dissolution leading to a saturated interface occurs almost instantly when the lanthanide or Pu melts, followed immediately by precipitation and growth of the intermetallic. Further Be attack (i.e., in-growth of the intermetallic) is controlled by Be transport through the growing intermetallic and will be accompanied by some dissolution of the MBe_{13} layer.

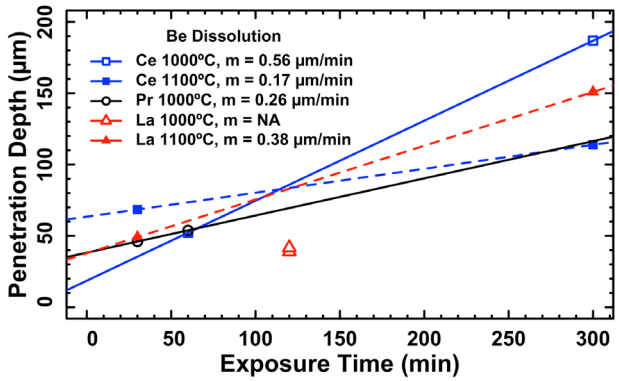

Figure 12. Penetration depth of intermetallic into the Be wall as a function of exposure time for Ce, Pr, and La melted in Be crucibles.

For comparison, the penetration depth of molten $PuBe_{13}$ into a Be crucible wall is reproduced from [9] in Figure 13. The calculated attack rate at 1000˚C is roughly 9 mil/hr (3.8 µm/min) and at 1100˚C it is approximately 16 mils/hr (6.7 µm/min). While the experimental conditions are not identical to those of the lanthanide experiments, the data indicate that the reactivity of Pu and the reactivity of some of the lanthanides are similar.

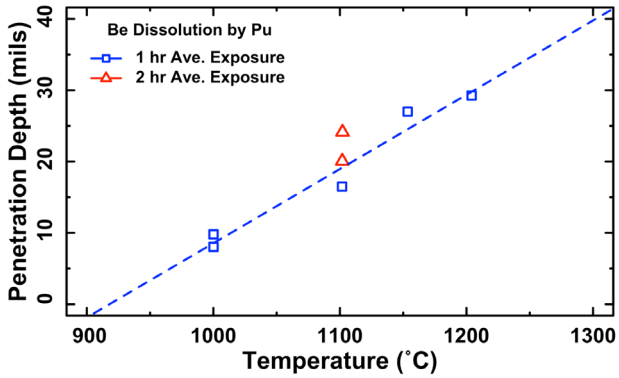

Figure 13. Penetration depth of the $PuBe_{13}$ intermetallic into the Be wall as a function of exposure temperature for two exposure times (replotted from [9]).

3.5 Monitoring the Be-Pu Reaction via Neutron Production

The final important piece of information in describing the Be and Pu (and similarly, other lanthanides) interaction is to identify when Be dissolution and intermetallic formation begin. Neutron count rate spectra can be used to make these determinations for studies involving Pu because the reaction between Be and Pu, in particular $PuBe_{13}$ formation, produces large quantities of neutrons (α-n reaction). Observations made during Be-Pu experiments can be extended to Be-lanthanide reactions.

Figure 14-Figure 17 show the neutron count rates and sample temperatures as a function of time for a number of representative tests. In every test case, the neutron count rate profiles have similar aspects. These include (1) an initial count of the background during heat-up; (2) a rapid increase in the neutron count rate at approximately the Pu melting point (640˚C) due to the initiation of the α-n reaction; (3) a change in slope in the neutron count rate as the hold temperature is reached; and (4) a relatively constant slope until the furnace temperature is decreased, resulting in (5) a decrease in the neutron counts until the solidification temperature is reached, where the neutron count rate stabilizes to a constant rate. The decrease and stabilization of the count rate with solidification indicates that a runaway reaction will not occur.

Temperature, exposure time, and furnace ramp rate effects on $PuBe_{13}$ formation can be assessed by comparing the plots in Figure 14-Figure 17. Exposure time at a specific temperature does not appear to greatly affect the neutron count rate—the neutron count rate during heat-up for the 1-hr exposure at 1000˚C (Figure 14) and the neutron count rate for the 2-hr exposure at 1000˚C (Figure 15) are roughly equal, but the count rates at the hold temperature vary slightly. Similarly, the total neutron counts for the 1-hr test are higher than for the 2-hr test. These variations are likely caused by the reaction of residual material at the edge of the crucible. No conclusion can be drawn about the correlation between neutron count rate and $PuBe_{13}$ thickness at this time, due to a lack of micrographs.

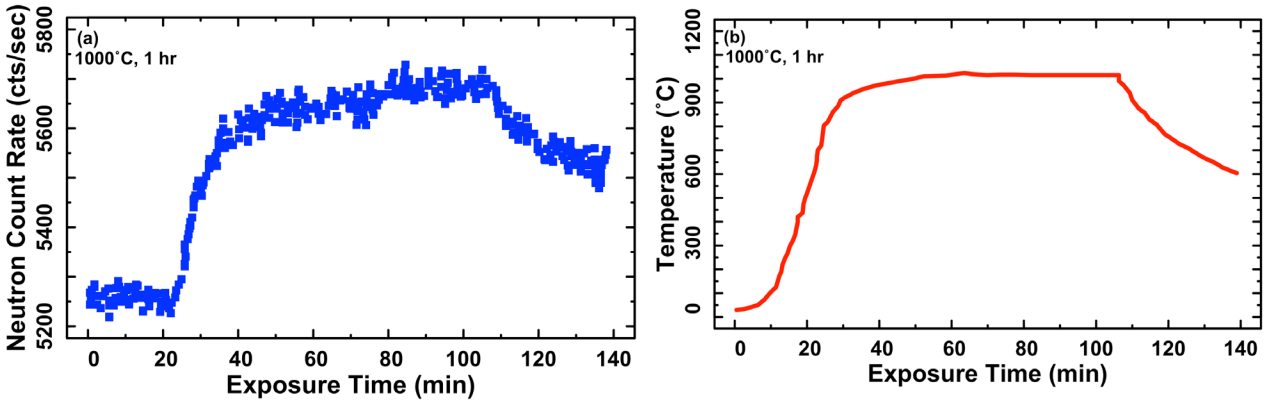

Figure 14. Neutron count rate vs. time (a) and temperature vs. time (b) plots for 57 g of Pu alloy melted in a Be crucible and held at 1000˚C for 1 hr. The heating rate for this test was 40˚C/sec. The initial neutron rate during heat-up (~20–40 mins) was roughly 30 cts/sec/min (the slope of the increasing portion of the curve); the steady-state rate was ~0.88 cts/sec/min, and the rate during cooldown was about 5 cts/sec/min.

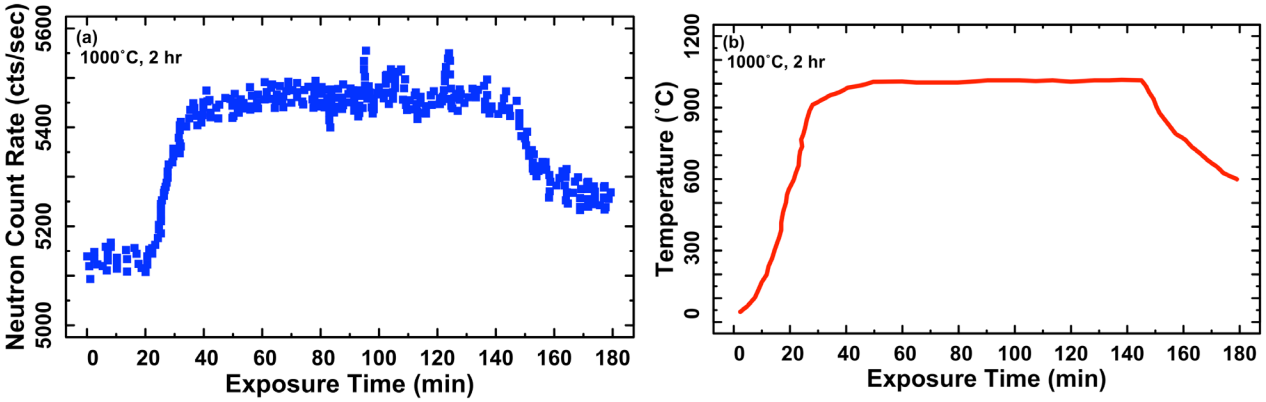

Figure 15. Neutron count rate vs. time (a) and temperature vs. time (b) plots for 57 g of Pu alloy melted in a Be crucible and held at 1000˚C for 2 hr. The heating rate for this test was 40˚C/sec. The initial neutron rate during heat-up was roughly 30 cts/sec/min; the steady-state rate was ~0.13 cts/sec/min, and the rate during cooldown was about 10 cts/sec/min.

Conversely, decreasing the ramp rate to the hold temperature by 60% (Figure 16) leads to a roughly 50% decrease in the neutron count rate during heat-up (i.e., from ~30 cts/sec/min to ~15 cts/sec/min). The steady-state count rate at the hold temperature is similar to the count rates calculated for the two tests conducted at a faster ramp rate.

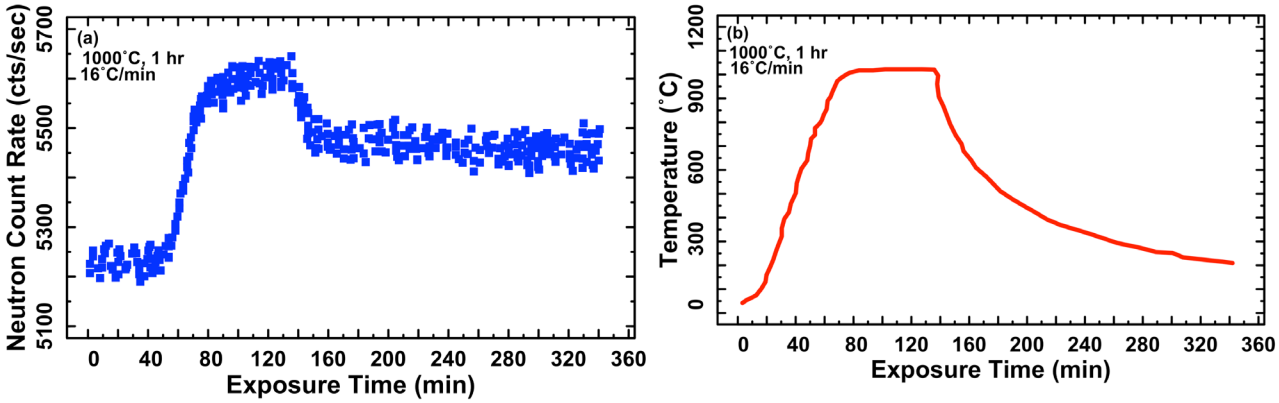

Figure 16. Neutron count rate vs. time (a) and temperature vs. time (b) plots for 57 g of Pu alloy melted in a Be crucible and held at 1000˚C for 1 hr. The heating rate for this test was 16˚C/sec. The initial neutron rate during heat-up is roughly 15 neutrons/min; the steady-state rate is ~0.5 cts/sec/min, the rate during cooldown is about 8 cts/sec/min, and the rate after solidification (t > 160 min) is roughly 0.13 cts/sec/min.

Changing the hold temperature also affects the neutron count rate values, as shown in Figure 17. In this case, the furnace is ramped to 1200˚C and held for 2 hr. The count rate during heat-up is initially about 10 cts/sec/min; at 80 min there is a visible dip in the count rate, followed by a decrease in the slope to about 3 cts/sec/min. Postmortem examination of the crucible revealed a pinhole leak that initiated where the thermocouple attached to the bottom of the crucible (Figure 2). The release of the small amount of molten material could change the geometry of the system sufficiently to affect neutron count rates.

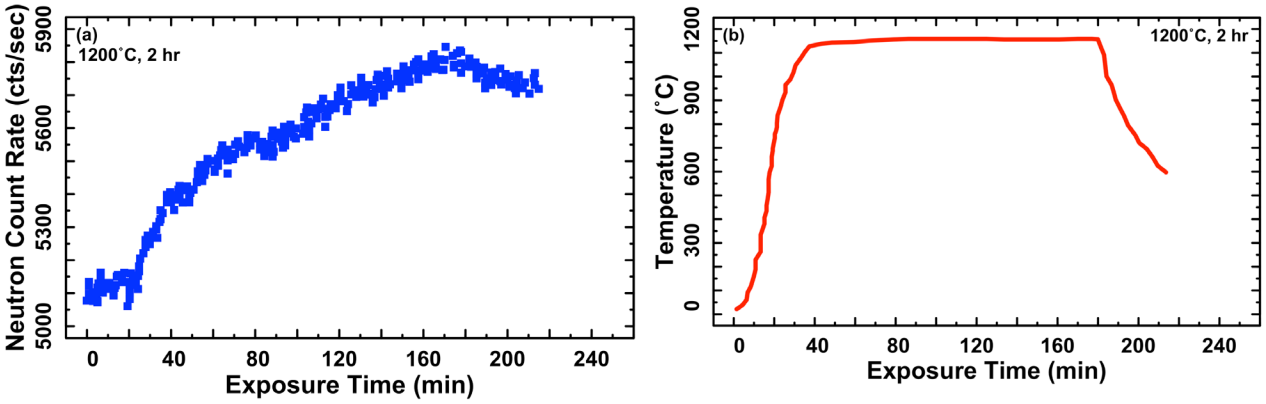

Figure 17. Neutron count rate vs. time (a) and temperature vs. time (b) plots for 57 g of Pu alloy melted in a Be crucible and held at 1200˚C for 2 hr. The heating rate for this test was 40˚C/sec. The initial neutron rate during heat-up was roughly 10 cts/sec/min. After the dip at ~80 min, the rate decreased to ~3 cts/sec/min. A steady-state rate is not obvious; the rate during the short cooldown was about 4 cts/sec/min.

4 Discussion

While the metallographic and kinetic data compiled in this review report are incomplete, a number of comparisons can be drawn between lanthanide and actinide interactions with the alkaline earth metal Be, especially when neutron count rate data collected during Be exposure to Pu are considered.

The micrographs assessed during this review suggest that intermetallic formation in the Pu-Be system is not well modelled by a single lanthanide-Be system, but rather displays elements in common with multiple systems. Two key microstructural features are evident in micrographs of the Pu-Be system (Figure 7): significant porosity at the Be-$PuBe_{13}$ interface and large, blocky dendrites at the $PuBe_{13}$-Pu interface. Significant porosity (i.e., vacancy accumulation) is also observed along the Be-intermetallic interface in the Yb-Be system (Figure 5), but no dendrites are formed, and Be dissolution is minimal. Vacancy accumulation and a planar interface suggest that the intermetallic growth is controlled by Be diffusion across the intermetallic through a Kirkendall effect and that constitutional gradients are minimal. Conversely, large constitutional dendrites are observed in the Ce, Sm, and Pr-Be systems (Figure 3, Figure 4, Figure 6), with significant Be dissolution and negligible vacancy formation behind the intermetallic. These characteristics suggest that countercurrent diffusion is active in these systems. Clearly then, the mechanism of $PuBe_{13}$ formation is complex and depends both on composition gradients (hence the constitutional dendrite

formation) [9] driven by Be attack and dissolution and on the growth of Be diffusion at elevated temperature across the intermetallic.

Incorporating neutron flux data from Pu-Be experiments (Figure 14-Figure 17) lends further insight into the mechanism of intermetallic formation. Prior to melting and subsequent flow of the molten Pu into the Be crucible, the neutron count rate is effectively constant at a background level (~5200 cts/sec). However, as the temperature increases above the Pu melting point, a significant linear rise occurs in the neutron rate, on the order of 10–30 neutrons per sec per min of exposure time. This increase may be due to an initial rapid interfacial Be dissolution into the liquid Pu, causing a significant increase in the number of α-n reactions, thereby generating a large increase in the sample's neutron production. Note that intermetallic formation requires only that the liquid be saturated at the interface, which may occur almost instantly upon melting and exposure. Therefore, the steep increase in neutron count rate is likely closely linked with the formation of $PuBe_{13}$. The neutron count rate stabilizes when the hold temperature is reached, suggesting that the reaction slows considerably after formation of a continuous layer and that continued growth is limited by diffusion of Be through the $PuBe_{13}$. Once the furnace power is turned off, the sample temperature decreases during cooling, and a rapid decrease is seen in the neutron count rate. This decrease in count rate is possibly due to precipitation of $PuBe_{13}$ from the now supersaturated liquid. Indeed, "islands" of $PuBe_{13}$ are observed in the solidified Pu matrix in Figure 7; similarly, large particles are formed in the denuded zone of the former liquid of the Sm-Be system (Figure 4), suggesting precipitation upon cooling. Upon complete solidification, the neutron count rate stabilizes at a value between the peak and background count rates (Figure 16). Tate and Coffinberry [8] have shown that the neutron output is maximized with solid solutions of the Pu-Be system, while $PuBe_{13}$ and mixtures of $PuBe_{13}$ precipitates within the Pu metal have lower neutron outputs. The net decrease in the neutron output from the sample will depend on the geometry of the sample and the precipitate size in the solidified liquid.

5 Summary & Recommendations

- Comparison of intermetallic morphologies highlights that the mechanism of $PuBe_{13}$ formation shares features in common with multiple rare-earth beryllides. In particular, the growth of constitutional dendrites reflects the formation of Be gradients during melting and intermetallic growth (as in Ce-Be, Sm-Be, Pr-Be systems). Additionally, vacancy accumulation behind the

intermetallic suggests that Be must diffuse through the intermetallic to react with additional molten metal (as in the Yb-Be system).

- Neutron production rate measurements during Pu-Be experiments reveal that Pu and presumably the lanthanides tested do not react with Be until melting. At that point, Be dissolution leads to liquid metal saturated with Be at the interface, followed by intermetallic formation. Solubility and diffusivity of Be in the lanthanide/actinide intermetallic control Be transport and correspondingly impact intermetallic growth rate and Be attack rate.

- Not all lanthanides follow the same kinetic trends. Sm, Yb, and likely Ce display parabolic intermetallic formation kinetics, while $PrBe_{13}$ is interface controlled. Some researchers have suggested that $PuBe_{13}$ growth may follow parabolic kinetics, but that was not directly calculable with the data in this report.

- In order to unambiguously determine the reaction kinetics of various lanthanide-Be compounds and compare those with actinide-Be compounds of interest, additional experiments are required. Intermetallic thickness and penetration depth as a function of time should be measured, in triplicate, at a minimum of three consistent temperatures.

6 Acknowledgements

This report is a compilation of data gathered over many years. The authors gratefully acknowledge the experimental and intellectual contributions of Dan Thoma of the University of Wisconsin-Madison (previously LANL), Loren Jacobsen, Ramiro Pereyra, Pallas Papin, Joseph L. Lowery, Bill Hutchinson, and Janice Aasen, all formerly with LANL, and Michelle Crown a past LANL student.

7 References

[1] H. Okamoto and L. Tanner, *Phase Diagrams of Binary Beryllium Alloys*, Metals Park, OH: ASM, 1987, pp. 165–168.

[2] E. Bucher, J. Maita, G. Hull, R. C. Fulton and A. S. Cooper, "Electronic Properties of the Beryllides of the Rare Earths and Some Actinides," *Physical Review B,* vol. 11, p. 440, 1975.

[3] W. B. Pearson, *Handbook of Lattice Spacings and Structures of Metals and Alloys*, New York: Pergamon, 1967.

[4] R. J. Hanrahan, Jr., T. G. Zocco, D. J. Thoma, L. A. Jacobsen, J. L. Lowery and R. Pereyra, "Surrogate Studies of the Pu-Be Reaction II," in *21st Aging Compatibility & Stockpile Stewardship Conference*, Albuquerque, 1997.

[5] T. G. Zocco, "Plutonium-Beryllium Reaction Studies: In-Situ Neutron and Metallographic Observation of the Plutonium-Beryllium Reaction," Unpublished Manuscript*,* 26 August 1996.

[6] G. F. Jones, M. Dong, C. O. Grigsby, W. B. Van der Heyden, and E. D. Dendy, "Transport and Chemical Reaction in the Plutonium-Beryllium Liquid Metal System," LA-UR-01-0400, Los Alamos, 2001.

[7] N. Zhao, Y. Zhong, M. L. Huang, H. T. Ma and W. Dong, "Growth kinetics of Cu6Sn5 intermetallic compound at liquid-solid interfaces in Cu/Sn/Cu interconnects under temperature gradient," *Scientific Reports,* vol. 5:13491, pp. 1–12, 2015.

[8] R. J. Hanrahan, Jr. and D. J. Thoma, "PFR Pu Surrogates for Be Compatibility Testing," Unpublished Manuscript, 1997.

[9] J. H. Steele and T. G. Zocco, "Attack Rate Studies of Liquid Pu on Be," in *Containment Workshop Presentations,* UCRL-MI-107490, Livermore, 1991.

[10] M. C. Flemings, *Solidification Processing*, Wiley-VCH Verlag GmbH & Co. KGaA, 1974.

[11] R. E. Tate and A. S. Coffinberry, "Plutonium-Beryllium Neutron Sources, Their Fabrication and Neutron Yield," in *Second United Nations International Conference on the Peaceful Uses of Atomic Energy*, A/Conf.15/P/700 , 1958.

8 Appendix: Additional Data

Lanthanum and a cerium-gallium alloy were melted in Be crucibles, and the thickness of the resulting intermetallic layers was measured from micrographs like those shown in Figure A1 and Figure A2. While insufficient data were collected to conduct a full kinetic analysis of intermetallic formation, thickness as a function of exposure time (Figure A3) was plotted to determine the most likely rate-determining steps. As evident in Figure A3, the fits to the data are somewhat poor, but based on curve shape and n values of 0.6 and 0.4 for La and CeGa, respectively, it is likely that diffusion controls intermetallic growth in both systems. Additionally, comparing the intermetallic

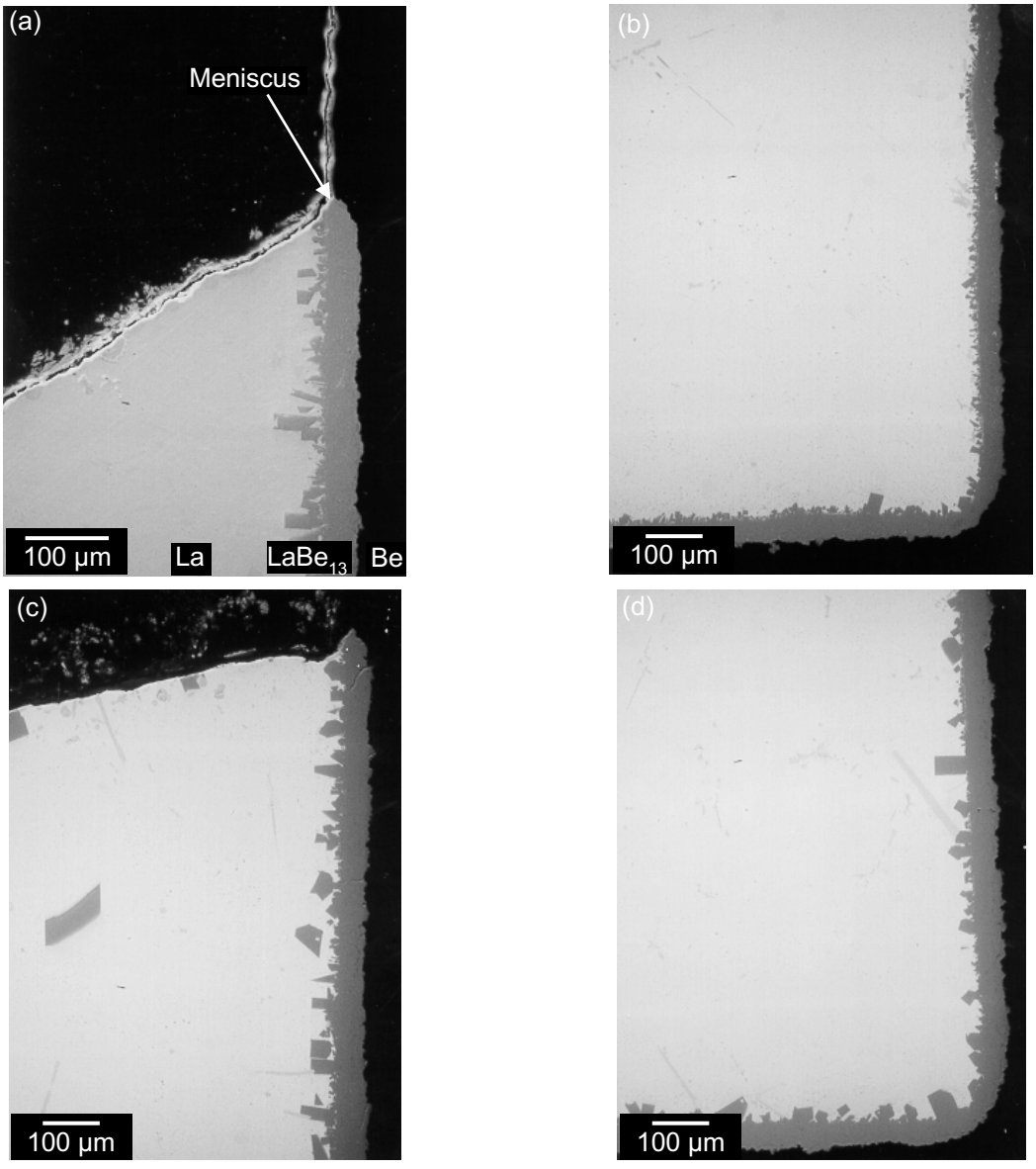

Figure A1. $LaBe_{13}$ growth at 1000°C (a-b) and 1100°C (c-d). The crucible is oriented vertically in all images.

thicknesses for the Ce-Be and CeGa-Be system (Table A2), it is apparent that the addition of Ga

depresses the reaction rate. This effect is likely caused by Ga altering the transport mechanism through the intermetallic.

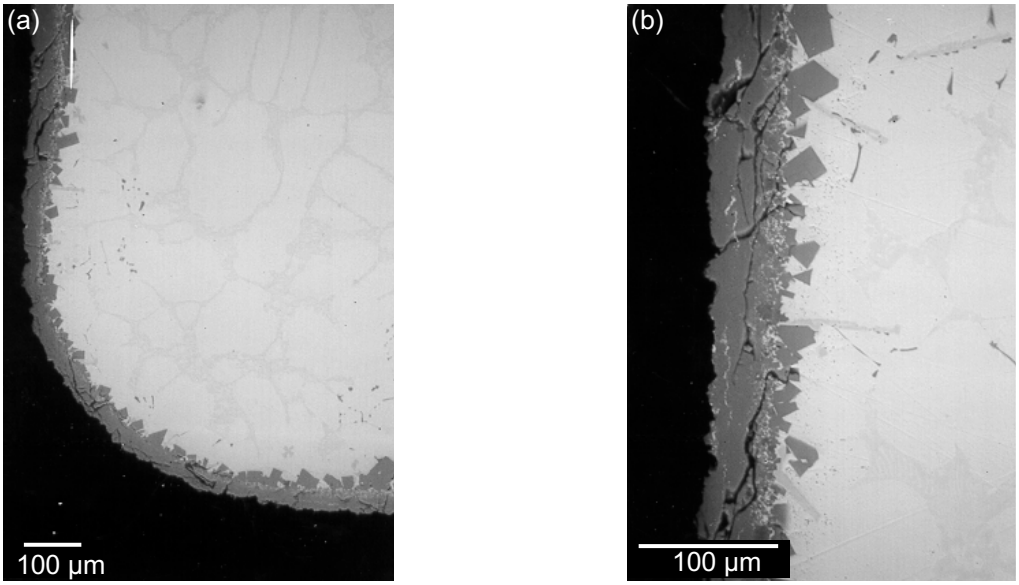

Figure A2. $CeGaBe_{13}$ growth at 1000˚C. The crucible is oriented vertically in both images.

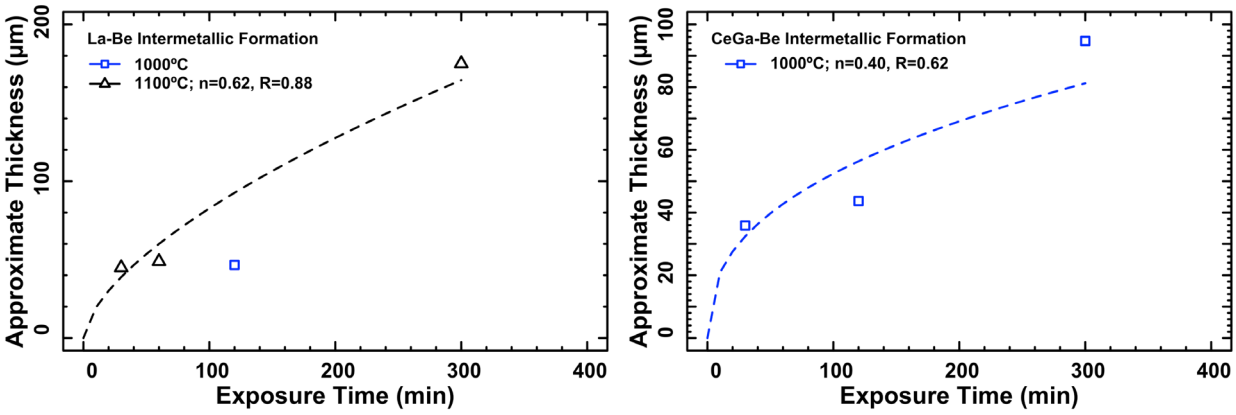

Figure A3. $LaBe_{13}$ (left) and $CeGaBe_{13}$ (right) growth at 1000˚C.

Table A1. MBe_{13} Intermetallic Layer Thickness as a Function of Exposure Temperature and Time for Each of Six M Components. (Double dashes indicate experiments were not conducted at a particular temperature/time.)

Rare Earth Element	**Exposure Temperature (˚C)**	**Thickness at 5 min (μm)**	**Thickness at 30 min (μm)**	**Thickness at 60 min (μm)**	**Thickness at 120 min (μm)**	**Thickness at 300 min (μm)**	**Thickness at 600 min (μm)**
Ce	*1000*	--	41.38	47.99	120.34	198.12	319.18
	1100	--	53.61	83.48	--	192.99	--
Sm	*1000*	5.81	15.7	20.34	--	54.41 (at 240 min)	--
	1100	--	30.21	31.12	55.98	80.70 (at 240 min)	--
Yb	*1000*	--	10.02	13.94	15.47	--	30.97
	1100	--	20.66	22.99	47.96	--	--
Pr	*1000*	6.70	46.37	72.79	--	388.32	--
	1100	--	40.10	60.37	--	418.22	--
La	*1000*	--	--	--	46.55	--	--
	1100	--	44.88	48.83	--	175.02	--
Ce/Ga	*1000*	--	35.88		43.66	94.72	--
	1100	--	--	--	--	--	--

Table A2. Penetration Depth of Molten Metal into Be Crucible Walls. (Dissolution rates are calculated from these data. Note that Pu penetration depth was originally measured in mils.)

Metal Element	**Exposure Temperature (˚C)**	**Penetration at 30 min (μm)**	**Penetration at 60 min (μm)**	**Penetration at 120 min (μm)**	**Penetration at 300 min (μm)**
Ce	*1000*	--	52.3	--	186.6
	1100	68.5	--	--	113.9
La	*1000*	--	--	40.3	--
	1100	49.2	--	--	150.9
Pr	*1000*	46.1	53.9	--	--
Pu	*1000*	--	238.8 (9.4mils)	--	--
	1100	--	419.1 (16.5mils)	561.3 (22.1 mils)	--
	1150	--	685.8 (27.0 mils)	--	--
	1200	--	744.2 (29.3 mils)	--	--


Los Alamos
NATIONAL LABORATORY
EST. 1943